Scientific paper

### Synthesis, Characterization, DFT Investigation and In Silico Anti-eczema Evaluation of a Novel Thiazolidinone Derivative

Amine Ould Rabah<sup>1</sup>, Abdelmadjid Benmohammed<sup>2,3</sup>, Abdelkader Chouaih<sup>1,\*</sup>, Meriem Goudjil<sup>4</sup>, Rachida Rahmani<sup>1,5</sup>, Nour El-Houda Belkafouf<sup>1</sup>, Mohammed Hadj-Mortada Belhachemi<sup>1</sup>, Fatima Zohra Boudjenane<sup>1</sup>, Ayada Djafri<sup>2</sup>, Nourdine Boukabcha<sup>1,6</sup>

<sup>1</sup> Laboratory of Technology and Solid Properties (LTPS), Abdelhamid Ibn Badis University of Mostaganem, 27000 Mostaganem, Algeria.

<sup>2</sup> Laboratory of Organic Applied Synthesis (LSOA), Department of Chemistry, Faculty of Sciences, University of Oran 1, Ahmed Ben Bella, 31000 Oran, Algeria.

<sup>3</sup> Chemistry Department, Faculty of Exact Sciences, Mustapha Stambouli University of Mascara, B.P. 763, 29000 Mascara, Algeria.

<sup>4</sup> Dipartimento di Scienze della Terra, Università degli Studi di Firenze, via G. La Pira 4, I-50121 Firenze, Italy.

<sup>5</sup> Department of Process Engineering, Faculty of Sciences and Technology, Ahmed Zabana - University of Relizane, Relizane, Algeria.

<sup>6</sup> Chemistry Department, Faculty of Exact Sciences and Informatics, Hassiba Benbouali University, 02000 Chlef, Algeria.

\* Corresponding author: E-mail: abdelkader.chouaih@univ-mosta.dz, achouaih@gmail.com

Received: 12-11-2024

#### **Abstract**

A new thiazolidinone derivative, (Z)-ethyl 2-((E)-2-((E)-(4-(methylthio)benzylidene)hydrazono)-4-oxo-3-phenylthiazolidin-5-ylidene)acetate (EMBTh), was synthesized using a condensation method. This study adopts a multidisciplinary approach, including the characterization of the compound through X-ray diffraction. A theoretical model for EMBTh has been established and validated by comparing the results of single-crystal X-ray diffraction (SC-XRD) with theoretical calculations from density functional theory (DFT). The molecule's electronic properties were analyzed using frontier molecular orbitals (FMO), which indicated an energy gap of 3.3 eV, suggesting good kinetic stability. The molecular electrostatic potential (MEP) identified nucleophilic regions near hydrogen atoms and electrophilic regions close to oxygen atoms. Additionally, intermolecular interactions were examined using a Hirshfeld surface analysis, showing that hydrogen contacts dominate, contributing 89.3%, which includes O···H/H···O, C···H/H···C, and H···H interactions. In contrast, examining intramolecular interactions through non-covalent interaction (NCI-RDG) analysis localized the van der Waals forces, highlighting the steric effects of the rings. Finally, a molecular docking study was performed to assess the anti-eczema potential of the EMBTh compound. The findings indicated a significant affinity for inhibiting the receptor (IL-4R $\alpha$ ), with a score of -7.2 kcal/mol, underscoring the therapeutic potential of EMBTh against the target protein involved in atopic eczema.

Keywords: Thiazolidinones; Molecular modeling; Non-covalent interactions; Molecular docking; Atopic eczema.

#### 1. Introduction

The synthesis and exploration of thiazole derivatives, particularly thiazolidinones, are crucial in medicinal chemistry due to their diverse pharmacological properties, including anti-inflammatory, antimicrobial, and antidia-

betic effects.<sup>1–3</sup> Although they possess a broad therapeutic potential, optimizing the biological activity and molecular stability of new thiazolidinone derivatives remains a vibrant area of research. Thiazolidinones, characterized by a five-membered ring containing nitrogen and sulfur atoms,

offer unique electronic and structural properties crucial for drug design. Incorporating sulfur atoms promotes the formation of low C-S  $\sigma^*$  orbitals, creating regions of low electron density known as σ-holes, which are essential for noncovalent biological interactions.<sup>4,5</sup> In addition, the  $\pi$ -electron delocalization within the thiazole ring enhances the stability and reactivity of these molecules, making them invaluable scaffolds in pharmaceutical research.<sup>6</sup> Recent studies underscore the significance of thiazolidinones in addressing critical health challenges, particularly inflammatory and autoimmune diseases.<sup>7</sup> Nevertheless, the application of thiazolidinones in treating dermatological conditions, such as eczema, remains largely unexplored. This gap highlights the necessity for novel thiazolidinone derivatives designed to target specific pathological pathways effectively.

This study introduces a novel thiazolidinone derivative, (*Z*)-ethyl 2-((*E*)-2-((*E*)-(4-(methylthio)benzylidene) hydrazono)-4-oxo-3-phenylthiazolidin-5-ylidene)acetate (EMBTh) designed to exhibit enhanced pharmacokinetic properties due to the strategic addition of benzylideneamino and methylthio groups.8 Besides, a comprehensive characterization of the molecular and electronic structure of EMBTh, its stability, and biological activity employing experimental methods such as single-crystal X-ray diffraction (SC-XRD), IR, UV-Vis, and NMR spectroscopic techniques combined with theoretical computational methods using density functional theory (DFT) calculations, in addition the biological activity of EMBTh was evaluated, focusing on its interactions with key molecular targets involved in the pathogenesis of eczema. 9-11 Especially, since most existing studies have focused on the antimicrobial and anti-inflammatory potential of thiazolidinones without investigating their interactions with specific dermatological targets. This study aims to bridge this gap by elucidating the interaction mechanisms of EMBTh with IL-4Ra, a key receptor implicated in the inflammatory pathway of eczema, thus offering a targeted therapeutic approach. The methodological innovations of this study include the use of cutting-edge spectroscopic and crystallographic techniques and recent simulation software. Additionally, the interdisciplinary nature of this work, which intersects fields like computational chemistry and molecular biology, broadens its scientific relevance.

# 2. Experimental and Computational Methods

#### 2. 1. Synthesis and Characterization

Synthesis of (Z)-ethyl 2-((E)-2-((E)-(4-(methylthio)benzylidene)hydrazono)-4-oxo-3-phenylthiazolidin-5-ylidene)acetate (EMBTh)

An equimolar mixture of (*E*)-2-(4-(methylthio)benzylidene)-*N*-phenylhydrazinecarbothioamide (1.5 mmol)

and diethyl acetylenedicarboxylate (1.5 mmol) in methanol (20 mL) was refluxed for 1 h. After completion of the reaction, the solution was cooled to room temperature. The yellow precipitate was collected by filtration and recrystallized using the solvents mixture EtOH/DMF.<sup>12</sup>

The thiazolidinone derivative was first characterized utilizing FT-IR and NMR methods. The IR spectrum was collected in a KBr pellet using a JASCO FT-IR 4200 Fourier Transform infrared spectrometer. The reported wavenumbers are expressed in cm $^{-1}$ . The NMR data were recorded for  $^{1}\mathrm{H}$  at 300 MHz and  $^{13}\mathrm{C}$  at 75 MHz in DMSO- $d_{6}$  with tetramethylsilane (Me<sub>4</sub>Si) using a Bruker AC 300P spectrometer (Bruker, Bremen, Germany).  $^{13}\mathrm{C}$  NMR chemical shifts are referred to the residual solvent peaks (39.6 ppm), while  $^{1}\mathrm{H}$  NMR chemical shifts are presented as ppm downfield from Me<sub>4</sub>Si.

### 2. 2. Single Crystal X-Ray Diffraction (SC-XRD) Analysis

The SC-XRD experiment was performed at room temperature ( $T=293~\rm K$ ) on a suitable yellow crystal mounted on the goniometer head of a Nonius Kappa CCD diffractometer operating with a monochromatic Mo Ka radiation ( $\lambda=0.71073~\rm \AA$ ). Instrument control, data processing, and data scaling were performed using the SAINT and SADABS programs implemented in Apex 2 software suite. The structure was determined by the intrinsic-phasing method using the ShelXT program and subsequently refined by full-matrix least-squares analyses based on  $F^2$  with ShelXL implemented in Olex  $2.^{14-16}$  Hydrogen atoms were placed at calculated positions, and their iso-

**Table 1.** Crystal data and structure refinement parameters for EM-BTh.

Empirical formula	$C_{21}H_{19}N_3O_3S_2$
Formula weight	425.51
Temperature (K)	293(2)
Crystal system, Space group	Monoclinic, $P2_1/c$ (no.14)
a (Å)	17.4021(5)
b (Å)	5.36240(10)
c (Å)	21.8298(8)
β (°)	95.7970(10)
Volume (ų)	2026.67(10)
Z	4
$\rho_{calc}$ (g/cm <sup>3</sup> )	1.398
$\mu  (\text{mm}^{-1})$	0.291
F(000)	892
Reflections collected	15747
Independent reflections	$4935 [R_{int} = 0.098]$
Data/restraints/parameters	4935/0/265
$R_1 [I \ge 2\sigma(I)], wR_2$	0.070, 0.131
$R_1$ [all data], $wR_2$	0.162, 0.167
Goodness-of-fit on $F^2$	1.038
Largest diff. peak/hole (e Å-3)	+0.51/-0.45

tropic thermal factors were refined using the riding model following the atom to which they are bound. All non-hydrogen atoms were refined anisotropically. One outlier reflection (002) was omitted in the final refinement cycles. The crystallographic data and details on the refinement are provided in Table 1. CCDC-2301965 contains supplementary crystallographic data that can be obtained from the Cambridge Crystallographic Data Centre.

#### 2. 3. Computational Methodology

Density functional theory (DFT) is a commonly used method in quantum chemistry to study organic molecules. Among the various functionals available, the B3LYP has proved to be a particularly powerful functional in many previous studies.<sup>17,18</sup> In the present study, this functional was used for calculations by using the 6-311++G (d,p) basis set. The geometry optimization was performed using Spartan 14 V1.1.4 software. 19-21 In addition, nuclear magnetic resonance (NMR) chemical shifts were calculated using the same software. The chemical reactivity descriptors were calculated from HOMO (highest occupied molecular orbitals) and LUMO (lowest unoccupied molecular orbitals) energy values. The major contributions of molecular orbitals were calculated using the time-dependent density functional theory (TD-DFT). The Hirshfeld surface analysis was developed using the Crystal Explorer 17.5 software.<sup>22</sup> For molecular docking, the ligand-protein interaction was calculated and performed using AutoDock Vina software,<sup>23</sup> and the visualization and analysis of this interaction was carried out using the Discovery Studio Visualizer software. The target protein file was prepared using AutoDock Tools.24

#### 3. Results and Discussion

### 3. 1. Synthesis Results and Characterization Data

Following the synthesis described above, the EMBTh was obtained as shown in Scheme 1.

Yellow solid; mp 210 °C. IR (KBr)  $v_{\rm max}$  1720 (C=O), 1696 (C=O), 1604 (C=N) cm<sup>-1</sup>. <sup>1</sup>H NMR (DMSO- $d_6$ ): δ 8.40 (s, 1H, CH=N), 8.70 (d, 2H, J = 8.4 Hz, Ar-H), 7.58–7.44 (m, 5H, Ar-H), 7.33 (d, 2H, J = 8.4 Hz, Ar-H), 6.77 (s, 1H, C=CH), 4.28 (q, 2H, J = 7.1 Hz, CH<sub>2</sub>), 3.31 (s, 3H, CH<sub>3</sub>), 1.28 (t, 3H, J = 7.1 Hz, CH<sub>3</sub>). <sup>13</sup>C NMR (DMSO- $d_6$ ): δ 166.0 (C), 164.6 (C), 160.9 (C), 160.0 (CH), 143.5 (C),

142.1 (C), 134.7 (C), 130.3 (C), 129.6 (3CH), 128.9 (2CH), 128.7 (2CH), 126.0 (2CH), 115.6 (CH), 62.0 (CH<sub>2</sub>), 14.6 (CH<sub>3</sub>), 14.5 (CH<sub>3</sub>).

#### 3. 2. Structural Study

#### 3. 2. 1. X-Ray Structure

The atomic coordinates and their corresponding displacement parameters of the new thiazolidinone derivative EMBTh are listed in Tables S1 and S2. The X-ray molecular structure of EMBTh with the numbering diagram

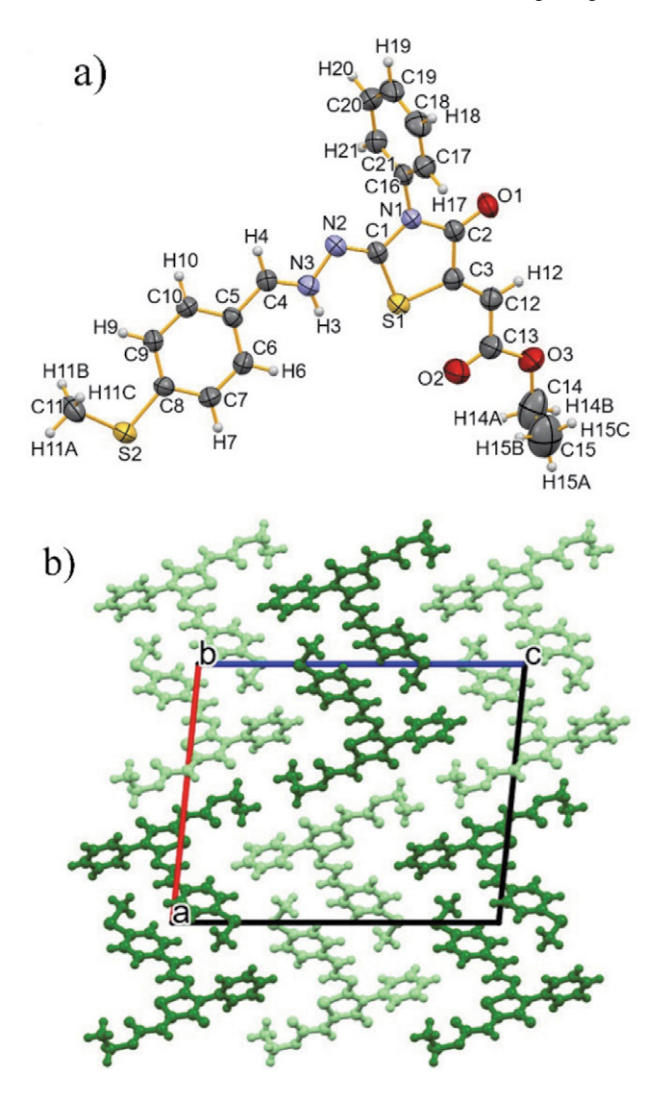


**Figure 1.** The asymmetric unit of EMBTh with ellipsoids represented at 50% probability level (a). Color code: C = grey, N = blue, O = red, S = yellow, H = cyan. (a). Ball and sticks representation along [010] showing T-shaped packed pairs (b).

is shown in Figure 1.a. The asymmetric unit contains one EMBTh molecule resembling a T-shaped motif similar to the skeletons of AGOMUG<sup>29</sup> and NIPPAF<sup>31</sup> thiazolidinone derivatives. The hydrazine bond N2–N3 connects the two main fragments of the molecule, with a bond length of 1.400(4) Å (see Table S3) which is shorter than that of the free hydrazine (1.447(2) Å). However, it is consistent with other quinolone derivatives containing hydrazine groups.  $^{25,26}$ 

The anisotropic displacement parameters of non-hydrogen atoms are within a consistent range except for C14 and C15 of the ethyl acetate group, which show higher factors (see Table S2). This is likely due to elevated thermal motion at room temperature since the Fourier difference map does not indicate any disorder. The molecule is stabilized by an intra-non-covalent S1...O2 interaction with a distance of 2.779(3) Å. The importance of this interaction, commonly ascribed to an  $n(O) \rightarrow \sigma^*$  interaction, is widely recognized in structural and medicinal chemistry. 5,27,28 The dihedral angles observed between the mean plane of oxothiazolidinone and the phenyl rings measure 12.27(11)° with C5-C10 and 69.94(12)° with C16-C21. Overall, the molecule is typically non-planar, and the phenyl ring planes of the ethyl-2-(4-oxo-3-phenylthiazolidin-5-yl)acetate and the 1-methyl-3-(methylthio)benzene fragments, respectively, are twisted relative to each other with a dihedral angle equal to 70.45(12)°. The crystal structure can be described as pairs of opposite EMBTh molecules generated via the inversion center, packed along the [010] direction (see Figure 1.b). One type of intermolecular contact, C-H...O, given in Table 2, contributes to the stabilization of the crystal packing, resulting in a 3D supramolecular architecture. This contact is observed between the oxygen atom that binds to the oxothiazolidine ring (acceptor) and the hydrogen atom of the phenyl ring C16-C21 (donor): C21-H21···O1, 2.545(2) Å/162.6(2)°, see Figure 2.

Table 2. Geometry of the C-H-··O bond (Å, °).

D-H···A	H···A	DA	D-H···A	Symmetry code
C21-H21···O1	2.545(2)	3.408(5)	162.6(2)	<i>x</i> ,1+ <i>y</i> , <i>z</i>

Due to their enhanced conformational flexibility, thiazolidinone derivatives can form diverse structural arrangements. When compared to similar crystal structures in the Cambridge database (AGOMUG,<sup>29</sup> MIZJUC,<sup>30</sup> NIPPAF,<sup>31</sup> and RIMDIC<sup>32</sup>), it is evident that EMBTh is primarily influenced by C–H···O bonds, similar to MIZJUC and NIPPAF. In contrast, AGOMUG and RIMDIC display additional interactions such as O–H···O, C–H···S, and N–H···O, highlighting how functional groups affect crystal reactivity. Furthermore, EMBTh does not show any incli-

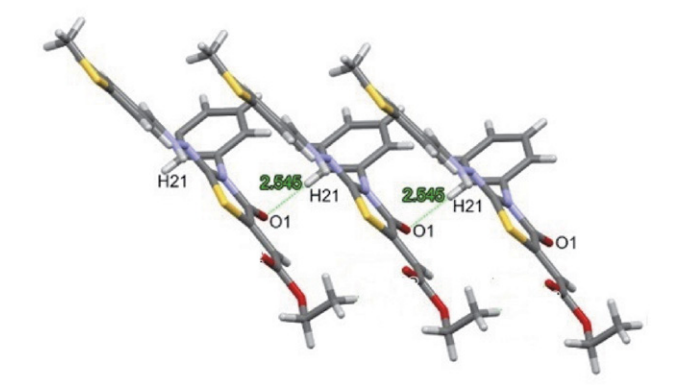


Figure 2. Intermolecular hydrogen bond interactions in EMBTh along the b-axis direction

nation towards dimer formation, unlike NIPPAF, which clearly exhibits molecular pair arrangements.

#### 3. 2. 2. Optimized Structure

The optimized structure of EMBTh is illustrated in Figure 3. The structural parameters, including bond lengths and angles, are presented in Table S3 and Table S4, which contain both experimental and theoretical data. The experimental results were obtained from SC-XRD measurements, while the theoretical data were calculated using the B3LYP/6-311++G (d,p) level of theory.<sup>33</sup> The mean absolute errors calculated for the majority of bond lengths and bond angles are 0.035 Å and 2°, respectively, demonstrating a strong similarity between theoretical and experimental results. This close agreement suggests the reliability and accuracy of the theoretical methods used. The most significant discrepancy is seen in the C14-C15 bond length, which is about 0.15 Å. The X-ray data suggests a delocalized character, while the DFT predicts a single bond character. The divergence observed can be attributed to the difference in the conditions used for experimental measurements (solid-state) and theoretical calculations

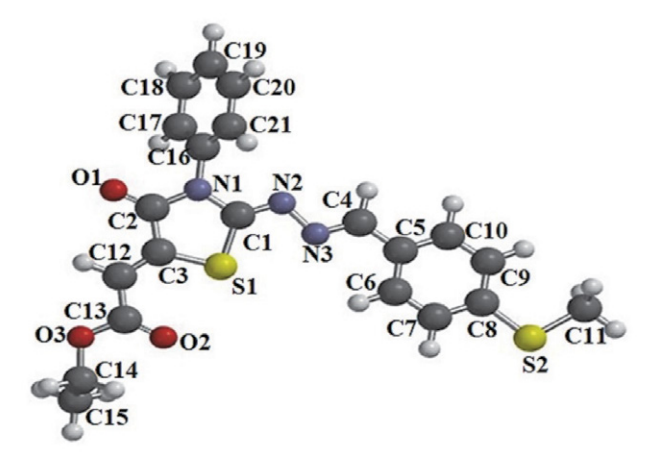


Figure 3. Optimized structure of EMBTh

(gaseous state).<sup>34</sup> Based on experimental and theoretical data, the two aromatic rings' C–C bond lengths range between 1.37 Å and 1.41 Å. These values align with those reported in the literature.<sup>27,28</sup> Analysis of the C–C bond lengths reveals a single bond character for C2–C3, C4–C5, and C12–C13, whereas a double bond character is observed for C3–C12. These results align well with existing literature data.<sup>35,36</sup> The average value of the thiazole cycle angles is 108°, corresponding to previous research.<sup>37</sup> The C15–C14–O3 bond angle in the studied molecule was experimentally determined to be 101.5°, while theoretical calculations predicted a value of 111.44°. This difference could be attributed to intermolecular interactions not accounted for in the theoretical calculations.

#### 3. 3. NMR Spectra Analysis

To further confirm the structure of EMBTh, its <sup>1</sup>H and <sup>13</sup>C NMR spectra were recorded. The experimental spectra are presented in Figure S1 (*see Supplementary information*). Table 3 lists both experimental and theoretical chemical shifts obtained by NMR analysis. The standard chemical shift for <sup>1</sup>H NMR in aromatic rings and C–H groups typically falls within the range of 6.00–8.00 ppm,<sup>38</sup> which aligns with the results obtained for the aromatic hydrogen atoms of the title compound. In contrast, the values obtained in the range of 0.96–4.93 ppm correspond to hydrogen atoms primarily associated with methyl or CH<sub>2</sub> groups, consistent with previous findings.<sup>26</sup> For <sup>13</sup>C NMR, the standard chemical shifts for aromatic carbon atoms are typically above 100 ppm,<sup>39</sup> which is consistent with the

values obtained for the aromatic carbons of the title compound, ranging from 127.43 to 133.98 ppm. However, shifts observed in the 142.92–172.16 ppm range are attributed to the electronegativity of neighboring atoms, primarily nitrogen, oxygen, and sulfur. Shifts below these ranges are primarily associated with CH, CH<sub>2</sub> groups, and methyl groups. The results obtained for <sup>1</sup>H and <sup>13</sup>C NMR exhibit a strong correlation between the theoretical and experimental data, aligning well with the standards established by previous research.

#### 3. 4. Hirshfeld Surface Analysis

Hirshfeld surface (HS) analysis characterizes the distribution of surface charges in molecular systems. This method visualizes the charge distribution using normalized contact distances ( $d_{\text{norm}}$ ), considering the van der Waals radius ( $r_i^{vdw}$  and  $r_e^{vdw}$ ) of the atoms involved in the analysis according to the following formula:

$$d_{norm} = \frac{d_i - r_i^{vdw}}{r_i^{vdw}} + \frac{d_e - r_e^{vdw}}{r_e^{vdw}}$$

where  $d_{(i)}$  and  $d_{(e)}$  are respectively the distances between the Hirshfeld surface and the nearest inner and outer atoms. The Hirshfeld surfaces plotted over  $d_{\text{norm}}$ ,  $d_{i}$ ,  $d_{e}$ , shape index and curvedness are illustrated in Figure 4 where the red colored areas represent the regions where atoms form intermolecular contacts shorter than the sum of their van der Waals radii, and the white color shows the bonds around the sum of the van der Waals radii, and the blue color shows the interactions, which are longer than

Atoms	<sup>13</sup> C-NMR isotr	opic chemical shifts	Atoms	<sup>1</sup> H-NMR Isotrop	ic chemical shifts
	Theoretical	Experimental		Theoretical	Experimental
C1	168.20	160.90	H4	8.41	8.40
C2	169.38	164.60	H6	7.92	7.33
C3	153.96	142.10	H7	7.08	8.70
C4	163.70	160.00	H9	6.94	8.70
C5	135.60	130.30	H10	7.31	7.33
C6	133.91	128.7	H11A	2.33	3.31
C7	127.43	126	H11B	2.22	3.31
C8	155.38	143.5	H11C	2.42	3.31
C9	127.43	126	H12	6.87	6.77
C10	133.91	128.7	H14A	4.93	4.28
C11	18.93	14.60	H14B	3.85	4.28
C12	120.53	115.6	H15A	1.27	1.28
C13	172.16	166.00	H15B	0.96	1.28
C14	64.75	62.00	H15C	1.72	1.28
C15	15.86	14.50	H17	7.52	7.58-7.44
C16	142.92	134.7	H18	7.61	7.58-7.44
C17	133.98	128.9	H19	7.55	7.58-7.44
C18	132.57	129.6	H20	7.56	7.58-7.44
C19	132.86	129.6	H21	7.51	7.58-7.44
C20	132.57	129.6			
C21	133.98	128.9			

the sum of the van der Waals radii. The shape index and curvedness diagrams allow to identify the morphology of the HS. In Figure 4, the shape index figure shows convex regions in blue color formed mainly by the carbon atoms of the aromatic rings and concave regions in red color formed mainly due to the carbon atoms of the molecule stacked above. The presence of two adjacent blue and red triangles shows the possibility of the presence of  $\pi-\pi$  bonds. The blue borders on the curvedness diagram show the planar  $\pi-\pi$  stacking of adjacent molecules. The intermolecular short contacts presented by red circles also called red spots involve strong hydrogen bonds of which two bonds are of type O···H/H···O illustrated in Figure 5 with a  $d_{\text{norm}}$  distance of 2.41 Å and the third bond is of type C···H/H···C with a  $d_{\text{norm}}$  distance of about 2.71 Å.

The quantitative analysis of the Hirshfeld surface illustrated by the fingerprint plot revealed a dominance of hydrogen bonds detailed in Table S3 with a total contribution of 89.3% which play a key role in the stabilization of the crystal packing, followed by bonds involving the C atom, which are mainly C...N/N...C, C...O/O...C, and C...C with a total contribution of about 9.1%. The main contributions of the different intermolecular contacts for EMBTh are displayed through the 2D fingerprint plots according to Figure S2. The contribution rate of the remaining bonds shown in the plot does not exceed 1.6%. All of these interactions contribute to the stability and organization of the crystal playing a crucial role in the structure and properties of the material.

#### 3. 5. NCI-RDG Analysis

Reduced density gradient (RDG) and non-covalent interaction (NCI) diagrams analyze non-covalent interac-

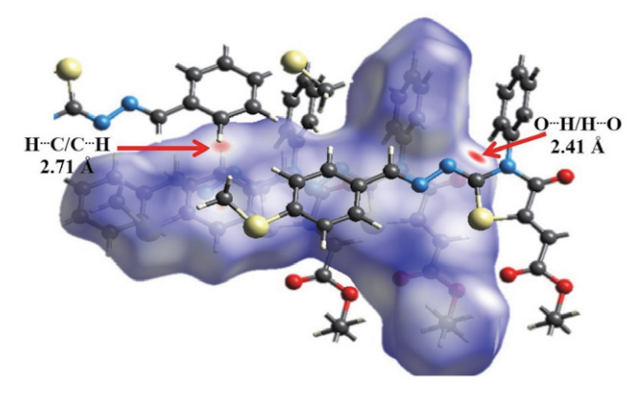
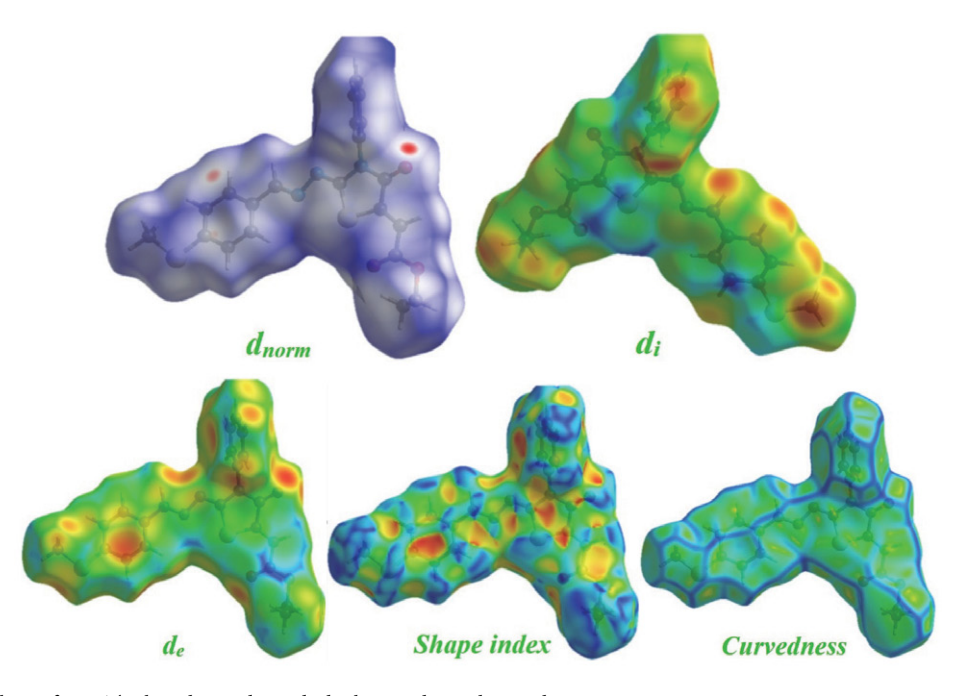


Figure 5. The 3D view of the Hirshfeld surface of EMBTh plotted over  $d_{\rm norm}.$ 

tions between molecules as a function of electron density multiplied by the sign of the second eigenvalue ( $\lambda 2$ )  $\rho$ , allowing strong and weak interactions to be differentiated. If the sign of  $(\lambda 2)$   $\rho$  is < 0, this indicates an attractive interaction while the sign of  $(\lambda 2) \rho > 0$  indicates a repulsive interaction, the values of  $(\lambda 2) \rho$  close to zero reflect a weak interaction of van der Waals.44-46 RDG scatter plots were obtained using Multiwfn software and the 3D isosurface is visualized using VMD software. 47,48 The NCI analyses were carried out by setting an isosurface value of 0.5 with an RDG isosurface range between -0.035 and 0.02 a.u. The 2D RDG diagrams and 3D isosurface are illustrated in Figure 6. The peaks observed in the RDG scatter plots are divided into three regions according to the values of sign  $(\lambda 2) \rho$ . The blue-colored region reflects strongly attractive interactions corresponding to strong hydrogen bonds, and the red color corresponds to strongly repulsive interac-



**Figure 4.** HS analysis of EMBTh plotted over  $d_{\text{norm}}$ ,  $d_{\text{i}}$ ,  $d_{\text{e}}$ , shape index and curvedness.

tions (steric effect), while the green-colored region is associated to weak interactions such as van der Waals interactions. 49 Figure 6 shows that the EMBTh exhibits a number of green and red spots. The red spots are observed in the middle of the aromatic rings and between adjacent electronegative atoms indicating a steric effect due to strong repulsions. However, the green spots identify the regions of weak van der Waals interactions observed between the oxygen atom and the hydrogen atom (O-H). Figure 6 also shows regions containing weak van der Waals interactions and repulsive interactions, represented by a single spot displaying red and green colors. However, the absence of the blue color indicates the absence of the strong attractive interactions generally associated to strong hydrogen bonds. Overall, the results of this analysis are consistent and complementary to those of the HS analysis, while also showing good agreement with the SC-XRD data.

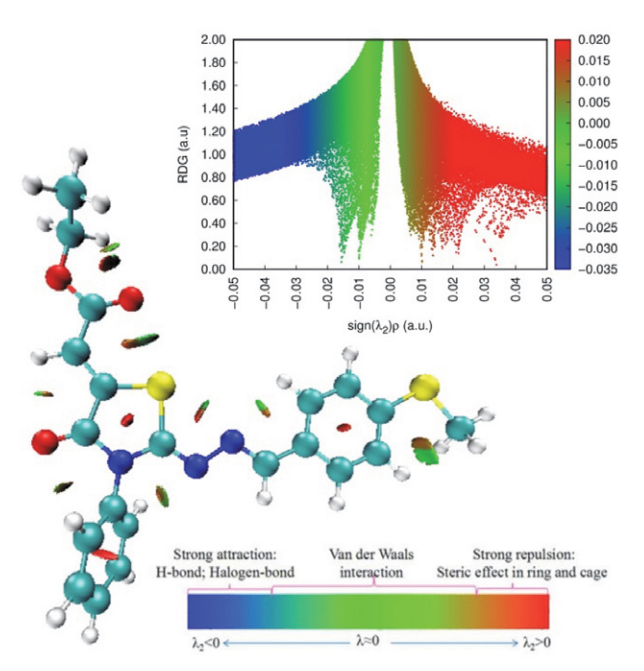


**Figure 6.** RDG scatter plots and 2D structure showing weak and strong interactions.

## 3. 6. HOMO-LUMO, TD-DFT Study and Chemical Reactivity Descriptors

The HOMO and LUMO are commonly referred to as frontier molecular orbitals. The HOMO orbital as an electron donor, while the LUMO, acting as an electron acceptor, can acquire an electron. Determining these parameters is crucial as it helps to assess various properties, such as kinetic stability and chemical reactivity. Figure 7 presents a HOMO-LUMO plot of the calculated frontier molecular orbitals using the B3LYP/6-311++G(d,p) basis set. As shown in Figure 7, the HOMO density is primarily concentrated on aromatic ring 2 and the adjacent sulfur atom. During the electron transition, electrons migrate to the

LUMO, mainly located on the thiazole ring and the adjacent carbonyl group. The positive and negative phases are depicted in red and blue, respectively. The calculated HO-MO-LUMO energy values for the molecule are –5.8 eV for the HOMO, –2.5 eV for the LUMO, and a band gap of 3.3 eV. This relatively large band gap indicates good kinetic stability for the studied molecule.<sup>52</sup>

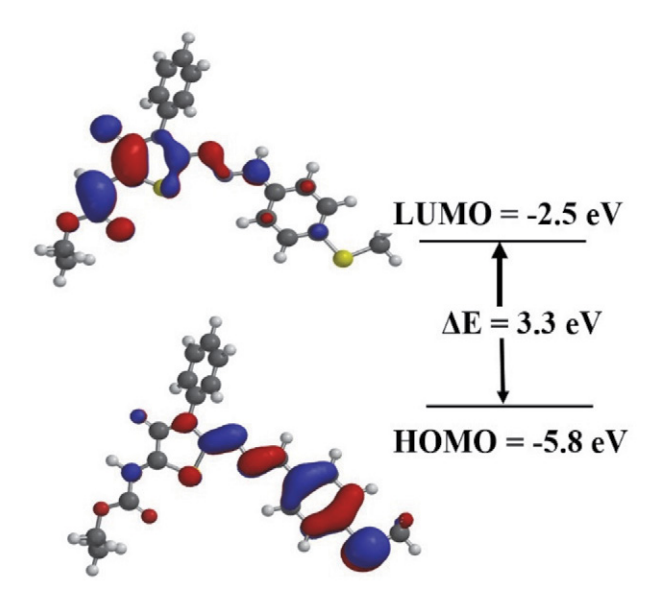


Figure 7. The HOMO-LUMO diagram of EMBTh.

The theoretical UV-visible spectroscopy study of the model identified two distinct absorption peaks in the visible spectrum region. The resulting transitions from this analysis have been characterized and presented in Table 4, specifying their wavelength, intensity, and respective percentage contribution. Indeed, the first peak observed at a wavelength  $\lambda = 326$  nm with an intensity of 0.8723 is associated with two electronic transitions, namely HOMO  $\rightarrow$ LUMO+1 and HOMO-1  $\rightarrow$  LUMO, with respective percentage contributions of 47% and 42%. The second peak observed at a wavelength  $\lambda = 414$  nm with an intensity of 0.4574 is associated with a HOMO  $\rightarrow$  LUMO electronic transition, with a contribution of 97%. These two peaks reflect the  $\pi \rightarrow \pi^*$  and  $n \rightarrow \pi^*$  transitions which might be due to the presence of free carbonyl groups and C=N double bonds and to the C=C double bond of aromatic rings.

The previously calculated HOMO and LUMO values are key elements in the determination of the chemical descriptors. Analysis of these descriptors can provide a deeper understanding of the kinetics and chemical reactivity of molecules, allowing for a more accurate evaluation of their behavior in the reaction environment and also to predict their potential reactions.<sup>53</sup> The most important descriptors have been calculated and presented in Table 5, including electronegativity, chemical potential, chemical hardness, and softness. The equations used to calculate these parameters have been referenced in previous work.<sup>54</sup> Firstly, a

**Table 4.** Theoretical electronic transitions, oscillator strength and major contributions for EMBTh.

B3LYP/6-311++G(d,p)		Major contributions			
λ (nm)	Intensity				
414.10	0.4574	HOMO →	LUMO	97%	
371.01	0.0046	HOMO-2 →	LUMO	89%	
326.30	0.8723	$HOMO \rightarrow$	LUMO+1	47%	
		HOMO-1 →	LUMO	42%	
323.41	0.0200	HOMO-3 →	LUMO	77%	
310.01	0.0041	HOMO-4 →	LUMO	54%	
		HOMO-8 →	LUMO	20%	
		HOMO-2 →	LUMO+1	18%	
307.73	0.1766	HOMO-2 →	LUMO+1	37%	
		$HOMO \rightarrow$	LUMO+1	18%	
		HOMO-1 →	LUMO	17%	

high ionization potential of 5.8 eV associated with a moderate electronegativity of 4.15 reveals relatively robust electron stability. Additionally, the negative chemical potential of –4.15 suggests a tendency to donate electrons rather than receive them. The hardness of 1.65 and relatively low overall softness of 0.606 indicate a moderate ability of the molecule to affect or be affected by electron bonds. Finally, the high electrophilic index of 5.218 reveals the molecule's tendency to act as an electrophilic center in chemical reactions. All these results suggest that the studied molecule is relatively stable with an electrophilic character.

**Table 5.** Calculated global chemical reactivity descriptors of EM-BTh.

Parameters (eV)	$B3LYP/6-311++G^{**}$	
E (HOMO)	-5.8	
E <sub>(LUMO)</sub>	-2.5	
ΔÈ	3.3	
p E <sub>A</sub>	5.8	
A	2.5	
	4.15	
	-4.15	
	1.65	
	0.61	
ı	5.22	
r.	7.50	
+	3.35	
	2.4	

#### 3. 7. Molecular Electrostatic Potential

The molecular electrostatic potential (MEP) of EM-BTh reveals important insights into the electron distribution across different functional groups of the molecule. Based on the optimized structure of EMBTh, the MEP distribution was computed (Figure S3). The methyl thioben-

zene group shows a region of low electron density around the sulfur atom, indicating its potential to act as an electrophilic site. In contrast, the oxothiazolidinone ring exhibits a more negative electrostatic potential, especially around the oxygen atom, suggesting that this area could participate in nucleophilic interactions. Additionally, the ethyl-2-(4-oxo-3-phenylthiazolidin-5-yl)acetate fragment highlights areas of significant negative potential near the carbonyl group, reflecting its importance in hydrogen bonding or interaction with positively charged species. The MEP map provides an overall understanding of how different regions of the molecule are likely to interact with other molecules, such as proteins or ligands, in molecular docking or chemical reactions.

#### 3. 8. Molecular Docking Studies

The biological activity was studied in two steps, the first one was to predict the adequate biological activity and the second one was to analyze the interaction between ligand and targeted protein. Inflammation is a vital mechanism of defense for human health, manifested by a complex immune system response involving several mediators including prostaglandins and interleukins through the blood vessels and lymphatic system, to quarantine or even eliminate the triggering factor, which may be bacteria, trauma, toxins, heat or any other reason. 55,56 However, any dysfunction of these immune cells can lead to a cascade of immune responses, which can be associated with numerous diseases, including chronic inflammatory diseases, cancer, autoimmune diseases etc, which explains the immense interest and importance of anti-inflammatory agents.<sup>57</sup> The medical need for anti-inflammatory agents to treat the wide range of diseases caused by alterations of these immune cells is far from satisfied. Until now, research and development in this field have been growing with the aim of obtaining a better efficacy/secondary effect ratio and even greater therapeutic benefits.<sup>58</sup> Recently, scientists have been working on thiazole derivatives. 59,60 Several studies have shown that thiazoles may be useful as anti-inflammatory drugs. 61-63 For example, the synthesis and evaluation of new diphenylthiazole derivatives as possible anti-inflammatory drugs,64 as well as all the other published studies,65-68 show that thiazoles may be useful as anti-inflammatory drugs. In the current study, we investigated the use of the EMBTh molecule as a potential therapeutic candidate against atopic eczema focusing on inflammatory skin diseases. Eczema, also known as atopic dermatitis (AD), is an inflammatory skin disease with a prevalence of about 15 to 30% in children and 2 to 10% in adults. Atopic dermatitis is more common in rural than urban areas due to environmental factors and genetic factors playing a role in the pathogenesis.<sup>69</sup> Atopic dermatitis is characterized by a skin barrier dysfunction, leading to an inflammatory im-

mune response that causes itching and scratching. By scratching, the skin barrier is further damaged, causing a more intense immune response, and this is the vicious cycle that people with eczema suffer from.<sup>70</sup> The immune response resulting from atopic dermatitis occurs in the Th2 pathway, specifically involving the cytokines IL-4 and IL-13, and therefore the interleukins IL-4, IL-13 and the α receptor of interleukin IL-4 (IL-4Rα) are the therapeutic targets for eczema.<sup>71</sup> In the second step, the docking of our molecule with eczema therapeutic targets (IL-4 and IL-4Ra) was calculated using the Auto-Dock Vina software.<sup>23</sup> Starting by downloading the IL-4 and IL-4Ra structures from the RCSB under the ID (1IAR).72 The choice of the active site was made based on the interaction sites of interleukin IL-4 and its receptor (IL-4Rα), this epitope of IL-4 and its receptor was defined by three parts, two of them have an amphipathic structure including hydrophobic bonds and hydrogen bonds, while the third part is marked by electrostatic bonds.<sup>73</sup> Therefore, the active site chosen for docking allows interaction with both IL-4 and its receptor alpha, hence inhibiting the IL-4 and IL-13 signaling process.<sup>71</sup> On AutoDock Vina software, the chosen active site was listed as following grid box parameters: a = 21.046, b =14.37, c = -16.759 and with centers of coordinates x =38, y = 26, z = 26. As listed in Table 6, several conformers were calculated of which the lowest energy is recorded at -7.2 kcal/mol.<sup>74</sup> The best pose for molecular docking with the lowest binding energy is shown in Figure S4. Interactions were analyzed using Accelrys Discovery

**Table 6.** AutoDock Vina results of the binding affinity and RMSD values for EMBTh.

Mode	Affinity (kcal/mol)	Rms dl.b.	Rms du.b.
1	-7.20	0	0
2	-6.6	20.65	22.888
3	-6.4	4.635	6.634
4	-6.4	3.569	4.502
5	-6.3	23.423	26.238
6	-6.2	21.189	24.61
7	-6.2	4.159	7.819
8	-6.1	20.981	24.675
9	-6.1	20.968	24.363

Studio software.<sup>75</sup> This analysis revealed a total of six bonds (Table 7) including two hydrogen bonds and two electrostatic bonds, while the last two bonds were hydrophobic.

Figure 8 displays the 3D intermolecular bound interactions involving the IL-4 protein. The first hydrogen bond is conventional linking the O2 atom of the molecule to the amino acid Arg88 of IL-4 at a distance of 3.398 (Å), and the second is  $\pi$ -donor linking Ring1 to Tyr74 of IL-4R $\alpha$  receptor at a distance of 4.057 (Å).

Molecular docking studies have demonstrated that EMBTh fits well within the active site of the IL-4R $\alpha$  receptor, establishing stable and specific interactions with key amino acid residues. These interactions—primarily hydrogen bonds, hydrophobic contacts, and van der Waals forces—suggest a strong binding affinity, which may contribute to the effective inhibition of the receptor's activity. This indicates the potential of EMBTh as a promising candidate for the treatment of eczema through modulation of IL-4R $\alpha$ -mediated inflammatory pathways.

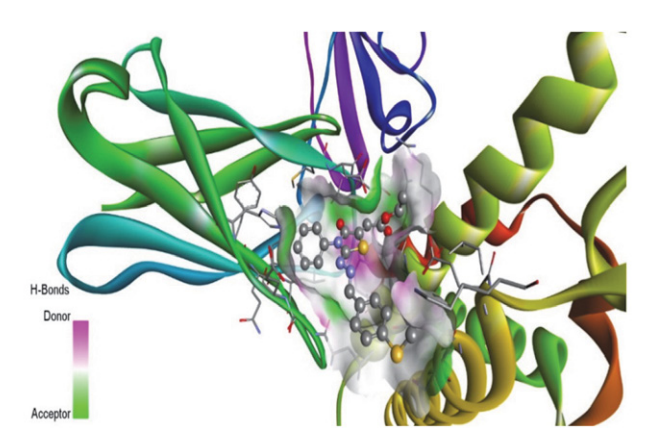


Figure 8. 3D ribbon structure of receptor/IL-4 protein.

For electrostatic bonds, Ring1 is connected with both Arg88 of IL-4 and Asp66 of IL-4R $\alpha$  forming a distance of 4.169 (Å) and 3.823 (Å), respectively. The two remaining hydrophobic bonds are  $\pi$ -alkyl and  $\pi$ - $\sigma$  joining Ring3 and Ring2 of the ligand with Leu39 and Leu43 of the IL-4R $\alpha$  receptor, giving a distance of 4.742 (Å) and 3.619

Table 7. Bonds formed from the interactions of EMBTh with IL-4 and its receptors.

Protein	Residue	Compound	Atom/group of compound	Category	Types	Distance (Å)
In re	ARG88	EMBTh	O <sub>2</sub> Atom	Hydrogen Bond	Conventional Hydrogen Bond	3.398
$\bigcup E \circ F$	TYR74		Ring3	Hydrogen Bond	π–Donor Hydrogen Bond	4.057
	ARG88		Ring1	Electrostatic	π–Ċation	4.169
ıkiı or a om	ASP66		Ring1	Electrostatic	$\pi$ –Anion	3.823
eukin-4 / tor alpha complex ID: 1IAR)	LEU39		Ring3	Hydrophobic	π–Alkyl	4.742
ha ha lex	LEU43		Ring2	Hydrophobic	π-σ	3.619

(Å), respectively. Figures 9 and 10 depict the intermolecular interactions between the IL-4 protein and the EMBTh ligand in 2D and 3D, respectively.

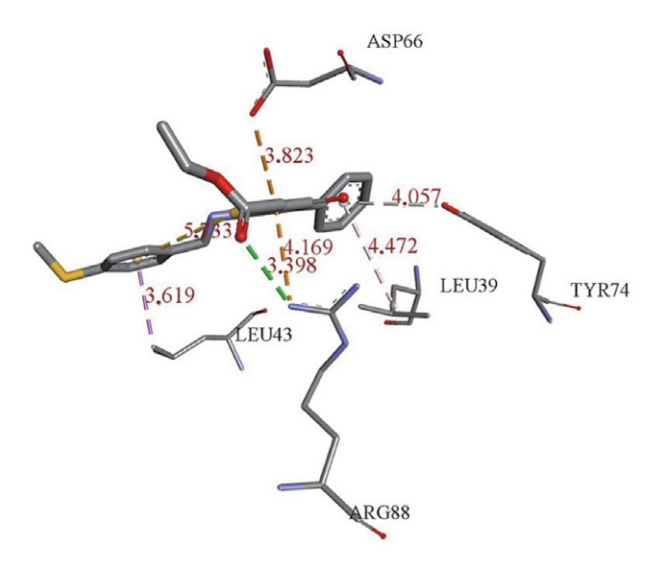


Figure 9. Interactions of EMBTh with IL-4 and its receptors.

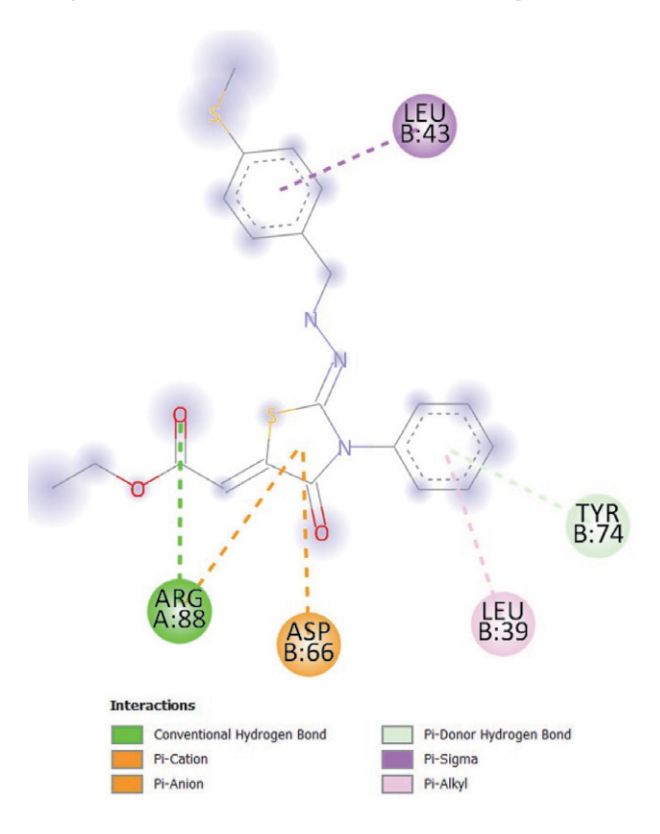


Figure 10: 2D interactions of the compound with IL-4 and its receptors.

#### 3. 9. Toxicity and Drug Likeness Investigation

Drug likeness and toxicity of the EMBTh compound were assessed using the ProTox-II server. ProTox II is a

virtual laboratory used to predict the toxicity of molecules. It integrates a combination of molecular similarity models and machine learning to analyze a multitude of parameters related to toxicity. 77,78 Based on the ADMET (Absorption, Distribution, Metabolism, Elimination, Toxicity) analysis, notably the Lipinski rules, 79 the studied molecule is in class 4 with an LD<sub>50</sub> of 1000 mg/kg (Table 8), which indicates good oral bioavailability.80 Table 9 presents a report of various toxicity parameters evaluated, including organ toxicity, cytotoxicity, carcinogenicity, mutagenicity, immunotoxicity and undesired effects pathways (Tox21) with their probabilities of being inactive, i.e. not toxic.81 The values show that four toxicity parameters were found inactive with a probability range of 0.54 to 0.62. These parameters include hepatotoxicity, carcinogenicity, mutagenicity and mitochondrial membrane stress response (MMP) pathways, while the other parameters assessed ranged in probability from 0.72 to 0.99, particularly immunotoxicity and cytotoxicity, which are directly related to the inflammatory response system and the immune system. These results are presented in the radar chart as shown in Figure S5. Finally, it was established that EMBTh is non-toxic regarding the targeted biological activity and it is suitable for oral administration.

Table 8. Lipinski's rules for EMBTh.

Parameter	Value
Toxicity Class	4
LD50	1000 mg/kg
Lipinski rule	0 violation
Molecular weight	425.52
Number of hydrogen bond acceptors	27
Number of hydrogen bond donors	0
Number of atoms	48
Number of bonds	50
Number of rotable bonds	7
Molecular refractivity	122.49
Topological Polar Surface Area	121.93
Octanol/water partition coefficient(logP)	4.39

#### 4. Conclusion

This study provides valuable insights into the structural and electronic properties of the newly synthesized compound EMBTh. Combined experimental and theoretical analyses confirm that EMBTh crystallizes in a monoclinic system,  $P2_1/c$ , exhibiting tight 3D supramolecular packing, including O···H, CH··· $\pi$  and  $\pi$ ··· $\pi$  interactions, contributing to its stability. The assessment of electronic behavior, using the DFT method with the B3LYP functional using the 6-311++G (d,p) basis set, reveals an energy gap of 3.3 eV and an electrophilic character, enhancing our understanding of the molecule's potential reactivity. The Hirshfeld surface and RDG isosurface density studies

Table 9. Report of the toxicity prediction.

Classification	Target	Prediction	Probability
Organ toxicity	Hepatotoxicity	Inactive	0.56
Toxicity end points	Immunotoxicity	Inactive	0.99
Toxicity end points	Cytotoxicity	Inactive	0.84
Toxicity end points	Carcinogenicity	Inactive	0.54
Toxicity end points	Mutagenicity	Inactive	0.54
Tox21-Nuclear receptor signalling pathways	Androgen Receptor Ligand Binding Domain (AR-LBD)	Inactive	0.96
Tox21-Nuclear receptor signalling pathways	Estrogen Receptor Ligand Binding Domain (ER-LBD)	Inactive	0.96
Tox21-Nuclear receptor signalling pathways	Androgen Receptor (AR)	Inactive	0.92
Tox21-Nuclear receptor signalling pathways	Peroxisome Proliferator Activated Receptor Gamma (PPAR-Gamma)	Inactive	0.85
Tox21-Nuclear receptor signalling pathways	Aromatase	Inactive	0.82
Tox21-Nuclear receptor signalling pathways	Estrogen Receptor Alpha (ER)	Inactive	0.82
Tox21-Nuclear receptor signalling pathways	Aryl hydrocarbon Receptor (AhR)	Inactive	0.72
Tox21-Stress response pathways	Nuclear factor (erythroid-derived 2)-like 2/ antioxidant responsive element (nrf2/ARE)	Inactive	0.85
Tox21-Stress response pathways	Heat shock factor response element (HSE)	Inactive	0.85
Tox21-Stress response pathways	ATPase family AAA domain-containing protein 5 (ATAD5)	Inactive	0.84
Tox21-Stress response pathways	Phosphoprotein (Tumor Supressor) p53	Inactive	0.80
Tox21-Stress response pathways	Mitochondrial Membrane Potential (MMP)	Inactive	0.62

revealed the contribution of the intermolecular interactions and their nature to the whole packing. Moreover, the significant docking affinity of -7.2 kcal/mol between EMBTh and the IL-4R $\alpha$  receptor suggests its potential as a therapeutic candidate for atopic eczema. By inhibiting the interaction between IL-4 and IL-4R $\alpha$ , EMBTh may effectively block the immune response cascade that contributes to the pathology of atopic dermatitis. These findings highlight the promise of EMBTh as a viable option for future therapeutic development in managing atopic conditions.

#### Supplementary Crystallographic Data

CCDC 2301965 contains supplementary crystallographic data for this paper. These data can be obtained free of charge from The Cambridge Crystallographic Data Centre via www.ccdc.cam.ac.uk/data\_request/cif, or by emailing data\_request@ccdc.cam.ac.uk, or by contacting The Cambridge Crystallographic Data Centre, 12, Union Road, Cambridge CB2 1EZ, UK; Fax: +44 1223 336033.

#### Acknowledgments

This study was supported by the Ministry of Higher Education and Scientific Research, and the General Directorate for Scientific Research and Technological Development (DG-RSDT). Abdelkader Chouaih expresses gratitude to the PCR (Pharmaco-Chimie Radicalaire) group, of the Faculté de Pharmacie, Aix-Marseille Université (France), for providing access to the X-ray diffraction facility.

#### 5. References

- Z. A. Muhammad, G. S. Masaret, M. M. Amin, M. A. Abdallah, T. A. Farghaly, *Med. Chem.* 2017, 13, 226–238.
   DOI:10.2174/1573406412666160920091146
- Y. Ali, M.S. Alam, H. Hamid, A. Husain, A. Dhulap, S. Bano, C. Kharbanda, *Bioorg. Med. Chem. Lett.* 2017, 27, 1017–1025. DOI:10.1016/j.bmcl.2016.12.069
- M. F. Ansari, S. M. Siddiqui, K. Ahmad, F. Avecilla, S. Dharavath, S. Gourinath, A. Azam, *Eur. J. Med. Chem.* 2016, 124, 393–406. DOI:10.1016/j.ejmech.2016.08.053
- S. Cascioferro, B. Parrino, D. Carbone, D. Schillaci, E. Giovannetti, G. Cirrincione, P. Diana, J. Med. Chem. 2020, 63, 7923–7956. DOI:10.1021/acs.jmedchem.9b01245
- B. R. Beno, K.-S. Yeung, M. D. Bartberger, L. D. Pennington, N. A. Meanwell, *J. Med. Chem.* 2015, 58 (11), 4383-4438.
   DOI:10.1021/jm501853m
- M. Alajarín, J. Cabrera, A. Pastor, P. Sánchez-Andrada, D. Bautista, J. Org. Chem. 2006, 71, 5328–5339.
   DOI:10.1021/jo060664c
- S. S. Abd El-Karim, H. S. Mohamed, M. F. Abdelhameed, A. El-Galil E. Amr, A. A. Almehizia, E. S. Nossier, *Bioorg. Chem.* 2021, *111*, 104827. DOI:10.1016/j.bioorg.2021.104827
- A. Nekrouf, K. Toubal, Y. Megrouss, N. E. H. Belkafouf, A. Djafri, N. Khelloul, J.-C. Daran, A. Djafri, A. Chouaih, *J. Mol. Struct.* 2022, *1262*, 133002.
   DOI:10.1016/j.molstruc.2022.133002
- K. Toubal, A. Djafri, A. Chouaih, A. Talbi, *Molecules*. 2012, 17, 3501–3509. DOI:10.3390/molecules17033501
- T. V. Shokol, N. V. Gorbulenko, A. V. Turov, V. P. Khilya, Chem. Heterocycl. Compd. 2013, 49, 325–330.

- **DOI:**10.1007/s10593-013-1250-0
- S. Saeed, N. Rashid, P. Jones, R. Hussain, M. Bhatti, Open Chem. 2010, 8, 550–558. DOI:10.2478/s11532-010-0014-2
- 12. A. Benmohammed, O. Khoumeri, A. Djafri, T. Terme, P. Vanelle, *Molecules*. **2014**, *19*, 3068–3083.
  - DOI:10.3390/molecules19033068
- 13. Bruker Analytical X-ray Systems, Inc, Apex2, Version 2 User Manual, M86–E01078, **2006**, 6, Madison, WI.
- G. M. Sheldrick, Acta Crystallogr. Sect. A. 2015, 71 (1), 3–8.
   DOI:10.1107/S2053273314026370
- G. M. Sheldrick, Acta Crystallogr. Sect. C Struct. Chem. 2015, 71 (1), 3–8. DOI:10.1107/S2053229614024218
- O. V. Dolomanov, L. J. Bourhis, R. J. Gildea, J. A. Howard, H. Puschmann, J. Appl. Crystallogr. 2009, 42(2), 339–341.
   DOI:10.1107/S0021889808042726
- A. D. Becke, J. Chem. Phys. 1993, 98, 5648–5652.
   DOI:10.1063/1.464913
- C. Lee, W. Yang, R. G. Parr, *Phys. Rev.* B. **1988**, *37*, 785–789.
   DOI:10.1103/PhysRevB.37.785
- W. J. Hehre, A guide to molecular mechanics and quantum chemical calculations, Wavefunction Inc., Irvine, California, USA, 2003.
- 20. Y. Shao, L. F. Molnar, Y. Jung, J. Kussmann, C. Ochsenfeld, S. T. Brown, A. T. B. Gilbert, L. V. Slipchenko, S. V. Levchenko, D. P. O'Neill, R. A. DiStasio Jr, R. C. Lochan, T. Wang, G. J. O. Beran, N. A. Besley, J. M. Herbert, C. Yeh Lin, T. Van Voorhis, S. Hung Chien, A. Sodt, R. P. Steele, V. A. Rassolov, P. E. Maslen, P. P. Korambath, R. D. Adamson, B. Austin, J. Baker, E. F. C. Byrd, H. Dachsel, R. J. Doerksen, A. Dreuw, B. D. Dunietz, A. D. Dutoi, T. R. Furlani, S. R. Gwaltney, A. Heyden, S. Hirata, C.-P. Hsu, G. Kedziora, R. Z. Khalliulin, P. Klunzinger, A. M. Lee, M. S. Lee, W. Liang, I. Lotan, N. Nair, B. Peters, E. I. Proynov, P. A. Pieniazek, Y. Min Rhee, J. Ritchie, E. Rosta, C. David Sherrill, A. C. Simmonett, J. E. Subotnik, H. Lee Woodcock III, W. Zhang, A. T. Bell, A. K. Chakraborty, D. M. Chipman, F. J. Keil, A. Warshel, W. J. Hehre, H. F. Schaefer III, J. Kong, A. I. Krylov, P. M. W. Gill, M. Head-Gordon, Phys. Chem. Chem. Phys. 2006, 8, 3172-3191. **DOI:**10.1039/B517914A
- P. Willoughby, S. Reisbick, *Protoc. Exch.* 2014, 10, 1–7.
   DOI:10.1038/protex.2014.015
- P. R. Spackman, M. J. Turner, J. J. McKinnon, S. K. Wolff, D. J. Grimwood, D. Jayatilaka, M. A. Spackman, J. Appl. Crystallogr. 2021, 54, 1006–1011. DOI:10.1107/S1600576721002910
- O. Trott, A. J. Olson, J. Comput. Chem. 2010, 31(2), 455–461.
   DOI:10.1002/jcc.21334
- G. M. Morris, R. Huey, W. Lindstrom, M. F. Sanner, R. K. Belew, D. S. Goodsell, A. J. Olson, *J. Comput. Chem.* 2009, 30, 2785–2791. DOI:10.1002/jcc.21256
- S. Eswaran, A. V. Adhikari, I. H. Chowdhury, N. K. Pal, K. D. Thomas, *Eur. J. Med. Chem.* 2010, 45, 3374–3383.
   DOI:10.1016/j.ejmech.2010.04.022
- O. Kourat, A. Djafri, N. Benhalima, Y. Megrouss, N. E. H. Belkafouf, R. Rahmani, J.-C. Daran, A. Djafri, A. Chouaih, *J. Mol. Struct.* 2020, 1222, 128952.
   DOI:10.1016/j.molstruc.2020.128952

- 27. M. H. M. Belhachemi, A. Benmohammed, H. Saiah, N. Boukabcha, M. Saidj, N. Dege, A. Djafri, A. Chouaih, *J. Mol. Struct.* **2022**, *1265*, 133342.
  - DOI:10.1016/j.molstruc.2022.133342
- 28. Y. Megrouss, F. Triki-Baara, N. Boukabcha, A. Chouaih, A. Hatzidimitriou, A. Djafri, F. Hamzaoui, *Acta Chim. Slov.* **2019**, *66*, 490–500. **DOI**:10.17344/acsi.2019.5066
- S. K. Mohamed, J. T. Mague, M. Akkurt, A. A. Hassan, M. R. Albayati, *Acta Crystallogr. Sect. E Struct. Reports Online* 2013, 69, o1553-o1554. DOI:10.1107/S1600536813025270
- J. T. Mague, M. Akkurt, S. K. Mohamed, A. A. Hassan, M. R. Albayati, *Acta Crystallogr. Sect. E Struct. Reports Online* 2014, 70, 0436–0437. DOI:10.1107/S1600536814007028
- J. T. Mague, M. Akkurt, S. K. Mohamed, A. A. Hassan, M. R. Albayati, *Acta Crystallogr. Sect. E Struct. Reports Online*. 2013, 69, o1401–o1402. DOI:10.1107/S1600536813021533
- S. K. Mohamed, M. Akkurt, J. T. Mague, A. A. Hassan, M. R. Albayati, *Acta Crystallogr. Sect. E Struct. Reports Online* 2013, 69, o1844–o1845. DOI:10.1107/S1600536813032042
- A. Ramalingam, M. Kuppusamy, S. Sambandam, M. Medimagh, O. E. Oyeneyin, A. Shanmugasundaram, N. Issaoui, N.D. Ojo, *Heliyon* 2022, 8, e10831.
   DOI:10.1016/j.heliyon.2022.e10831
- S. Gatfaoui, N. Issaoui, S. A. Brandán, M. Medimagh, O. Al-Dossary, T. Roisnel, H. Marouani, A. S. Kazachenko, *J. Mol. Struct.* 2022, 1250, 131720.
   DOI:10.1016/j.molstruc.2021.131720
- 35. A. Jamal, M. S. Haque Faizi, N. Dege, *J. Mol. Struct.* **2024**, *1300*, 137251. **DOI:**10.1016/j.molstruc.2023.137251
- N. Khelloul, K. Toubal, N. Benhalima, R. Rahmani, A. Chouaih, A. Djafri, F. Hamzaoui, *Acta. Chim. Slov.* 2016, 63, 619–626. DOI:10.17344/acsi.2016.2362
- N. E. H. Belkafouf, F. Triki Baara, A. Altomare, R. Rizzi, A. Chouaih, A. Djafri, F. Hamzaoui, *J. Mol. Struct.* **2019**, *1189*, 8–20. **DOI**:10.1016/j.molstruc.2019.04.028
- 38. K. Wolinski, J. F. Hinton, P. Pulay, *J. Am. Chem. Soc.* **1990**, *112*, 8251–8260. **DOI:**10.1021/ja00179a005
- N. Boukabcha, A. Djafri, Y. Megrouss, Ö. Tamer, D. Avcı, M. Tuna, N. Dege, A. Chouaih, Y. Atalay, A. Djafri, F. Hamzaoui, *J. Mol. Struct.* 2019, *1194*, 112–123.
   DOI:10.1016/j.molstruc.2019.05.074
  - M. Walton, J. M. Cox, C. A. Benson, D. (Dan) G. Patel, Y.-S. Chen, J. B. Benedict, *New J. Chem.* **2016**, *40*, 101–106. **DOI**:10.1039/C5NJ01718A
- Z. D. Benyahlou, F. Triki Baara, S. Yahiaoui, Y. Megrouss, N. Boukabcha, A. Djafri, A. Chouaih, A. Hatzidimitriou, *J. Mol. Struct.* 2023, 1277, 134781.
  - DOI:10.1016/j.molstruc.2022.134781
- R. Rahmani, A. Djafri, H. Khaldi, Y. Megrouss, A. R. Guerroudj, N. Dege, A. Djafri, A. Chouaih, *J. Mol. Struct.* 2025, 1320, 139661. DOI:10.1016/j.molstruc.2024.139661
- 42. S. Gatfaoui, N. Issaoui, T. Roisnel, H. Marouani, *J. Mol. Struct.* **2021**, *1225*, 129132. **DOI:**10.1016/j.molstruc.2020.129132
- B. Dutta, R. Purkait, S. Bhunia, S. Khan, C. Sinha, M. H. Mir, RSCAdv. 2019, 9, 38718–38723. DOI:10.1039/C9RA08614E
- 44. M. Saidj, A. Djafri, R. Rahmani, N. E. H. Belkafouf, N. Bou-

- kabcha, A. Djafri, A. Chouaih, *Polycycl. Aromat. Compd.* **2023**, *43*, 2152–2176. **DOI**:10.1080/10406638.2022.2039238
- E. R. Johnson, S. Keinan, P. Mori-Sánchez, J. Contreras-García, A. J. Cohen, W. Yang, *J. Am. Chem. Soc.* 2010, *132*, 6498–6506. DOI:10.1021/ja100936w
- B. Silvi, A. Savin, *Nature*. **1994**, *371*, 683–686.
   **DOI:**10.1038/371683a0
- 47. T. Lu, F. Chen, *J. Comput. Chem.* **2012**, *33*, 580–592. **DOI**:10.1002/jcc.22885
- 48. W. Humphrey, A. Dalke, K. Schulten, *J. Mol. Graph.* **1996**, *14*, 33–38. **DOI:**10.1016/0263-7855(96)00018-5
- F. Akman, A. Demirpolat, A.S. Kazachenko, A.S. Kazachenko, N. Issaoui, O. Al-Dossary, *Molecules* 2023, 28, 2684.
   DOI:10.3390/molecules28062684
- R. Rahmani, A. Djafri, A. Chouaih, A. Djafri, F. Hamzaoui, A. Krallafa, S. Afr. J. Chem. 2019, 72, 176–188.
   DOI:10.17159/0379-4350/2019/v72a23
- M. Mostefai, A. Benmohammed, N. Benhalima, N. Dege, R. Rahmani, O. Kourat, A. R. Guerroudj, A. Chouaih, A. Djafri, *J. Mol. Struct.* 2025, *1319*, 139308.
   DOI:10.1016/j.molstruc.2024.139308
- N. Boukabcha, A. Benmohammed, M. H. M. Belhachemi, M. Goudjil, S. Yahiaoui, Y. Megrouss, A. Djafri, N. Khelloul, Z. D. Benyehlou, A. Djafri, A. Chouaih, *J. Mol. Struct.* 2023, 1285, 135492. DOI:10.1016/j.molstruc.2023.135492
- R. Rahmani, F. Perveen, N. Benhalima, A. Djafri, N. Khelloul, A. Chouaih, A. Djafri, M. B. Kanoun, S. Goumri-Said, *J. Poly-cycl. Aromat. Compd.* 2023, 43(5), 4685–4706.
   DOI:10.1080/10406638.2022.2094971
- A. Benmohammed, M. Saidj, A. Djafri, A. R. Guerroudj, A. Ould Rabah, M. Goudjil, N. Boukabcha, A. Chouaih, A. Djafri, *J. Mol. Struct.* 2024, 136696.
   DOI:10.1016/j.molstruc.2023.136696
- C. Nathan, A. Ding, Cell. 2010, 140, 871–882.
   DOI:10.1016/j.cell.2010.02.029
- L. Chen, H. Deng, H. Cui, J. Fang, Z. Zuo, J. Deng, Y. Li, X. Wang, L. Zhao, *Oncotarget*. 2018, 9, 7204–7218.
   DOI:10.18632/oncotarget.23208
- 57. Y. Zhou, Y. Hong, H. Huang, *Kidney Blood Press. Res.* **2016**, *41*, 901–910. **DOI:**10.1159/000452591
- 58. M. F. Arshad, A. Alam, A. A. Alshammari, M. B. Alhazza, I. M. Alzimam, M. A. Alam, G. Mustafa, M. S. Ansari, A. M. Alotaibi, A. A. Alotaibi, S. Kumar, S. M. B. Asdaq, M. Imran, P. K. Deb, K. N. Venugopala, S. Jomah, *Molecules*. 2022, 27, 3994. DOI:10.3390/molecules27133994
- L. D. Khillare, M. R. Bhosle, A. R. Deshmukh, R. A. Mane, *Med. Chem. Res.* 2015, 24, 1380–1386.
   DOI:10.1007/s00044-014-1222-7
- B. Tiperciuc, A. Pârvu, R. Tamaian, C. Nastasă, I. Ionuţ, O. Oniga, *Arch. Pharm. Res.* 2013, 36, 702–714.
   DOI:10.1007/s12272-013-0083-9
- 61. J. Suh, E. K. Yum, H. G. Cheon, Y. S. Cho, *Chem. Biol. Drug Des.* **2012**, *80*, 89–98. **DOI:**10.1111/j.1747-0285.2012.01371.x
- M. E. Haiba, S. S. Abd El-Karim, R. S. Gouhar, M.I. El-Zahar,
   S. A. El-Awdan, *Med. Chem. Res.* 2014, 23, 3418–3435.
   DOI:10.1007/s00044-014-0926-z

- 63. V. Kamat, R. Santosh, B. Poojary, S. P. Nayak, B. K. Kumar, M. Sankaranarayanan, Faheem, S. Khanapure, D. A. Barretto, S. K. Vootla, ACS Omega. 2020, 5, 25228–25239.
  DOI:10.1021/acsomega.0c03386
- A. H. Abdelazeem, M. Habash, I. A. Maghrabi, M. O. Taha, *Med. Chem. Res.* 2015, 24, 3681–3695.
   DOI:10.1007/s00044-015-1418-5
- N. Chandak, P. Kumar, P. Kaushik, P. Varshney, C. Sharma, D. Kaushik, S. Jain, K. R. Aneja, P. K. Sharma, *J. Enzyme Inhib. Med. Chem.* 2014, 29, 476–484.
   DOI:10.3109/14756366.2013.805755
- 66. Y. E.-S. Sherif, A. A.-H. El-Asmy, M. Lotfy, *Croat. Chem. Acta.* **2012**, *85*(*1*), 19–26. **DOI:**10.5562/cca1802
- C. M. Moldovan, O. Oniga, A. Pârvu, B. Tiperciuc, P. Verite,
   A. Pîrnău, O. Crişan, M. Bojiţă, R. Pop, *Eur. J. Med. Chem.* 2011, 46, 526–534. DOI:10.1016/j.ejmech.2010.11.032
- R. D. Kamble, R. J. Meshram, S. V. Hese, R. A. More, S. S. Kamble, R. N. Gacche, B. S. Dawane, *Comput. Biol. Chem.* 2016, 61, 86–96. DOI:10.1016/j.compbiolchem.2016.01.007
- 69. Eczema StatPearls NCBI Bookshelf, (n.d.). https://www.ncbi.nlm.nih.gov/books/NBK538209/ (accessed November 28, 2022).
- P. Boudkova, E. Čermáková, J. Krejsek, J. Čelakovská, *Int. Immunopharmacol.* 2024, 136, 112327.
   DOI:10.1016/j.intimp.2024.112327
- 71. J. Di Lucca-Chrisment, M. Gilliet, *Rev. Med. Suisse.* **2018**, *14*, 685–689. **DOI**:10.53738/REVMED.2018.14.600.0685
- 72. RCSB PDB: Homepage, (n.d.). https://www.rcsb.org.
- 73. T. Hage, W. Sebald, P. Reinemer, *Cell* **1999**, *97*, 271–281. **DOI:**10.1016/S0092-8674(00)80736-9
- A. R. Guerroudj, N. Boukabcha, A. Benmohammed, N. Dege, N. E. H. Belkafouf, N. Khelloul, A. Djafri, A. Chouaih, *J. Mol. Struct.* 2021, *1240*, 130589.
   DOI:10.1016/j.molstruc.2021.130589
- 75. T.M. Karpiński, M. Kwaśniewski, M. Ożarowski, R. Alam, *Herba Pol.* **2021**, *67*, 1–8. **DOI:**10.2478/hepo-2021-0009
- M. Medimagh, N. Issaoui, S. Gatfaoui, S. Antonia Brandán,
   O. Al-Dossary, H. Marouani, M. J. Wojcik, *Heliyon* 2021, 7,
   e08204. DOI:10.1016/j.heliyon.2021.e08204
- M. N. Drwal, P. Banerjee, M. Dunkel, M. R. Wettig, R. Preissner, *Nucleic Acids Res.* 2014, 42, 53–58.
   DOI:10.1093/nar/gku401
- E. Oner, K. Al-Khafaji, M. H. Mezher, I. Demirhan, J. Suhail Wadi, E. Belge Kurutas, S. Yalin, K. Choowongkomon, *J. Biomol. Struct. Dyn.* 2023, 41(19), 9366–9381.
   DOI:10.1080/07391102.2022.2142848
- F. Z. Boudjenane, F. Triki-Baara, N. Boukabcha, N. E. H. Belkafouf, N. Dege, M. Saidj, N. Khelloul, A. Djafri, A. Chouaih, *J. Mol. Struct.* 2023, 1287, 135620.
   DOI:10.1016/j.molstruc.2023.135620
- S. Hammad, S. Bouaziz-Terrachet, R. Meghnem, D. Meziane, J. Mol. Model. 2020, 26, 160.
   DOI:10.1007/s00894-020-04408-2
- R. Rolta, D. Salaria, V. Kumar, C. N. Patel, A. Sourirajan, D. J. Baumler, K. Dev, *J. Biomol. Struct. Dyn.* 2022, 40, 3789–3803. DOI:10.1080/07391102.2020.1850364

#### **Povzetek**

S kondenzacijsko metodo smo pripravili nov derivat tiazolidinona, (*Z*)-etil 2-((*E*)-2-((*E*)-(4-(metiltio)benziliden)hidrazono)-4-okso-3-feniltiazolidin-5-iliden)acetate (EMBTh). Multidisciplinarna študija vključuje tudi karakterizacijo spojine z rentgensko difrakcijo. Poleg tega smo postavili teoretični model spojine EMBTh in ga validirali s pomočjo primerjave rezultatov rentgenske difrakcije monokristala (SC-XRD) z rezultati teoretičnih izračunov na osnovi teorije gostotnega potenciala (DFT). Elektronske lastnosti molekule smo analizirali na osnovi mejnih molekulskih orbital (FMO); energijska razlika 3,3 eV kaže na dobro kinetično stabilnost. Z določevanjem elektrostatskega potenciala molekule (MEP) smo identificirali nukleofilna območja v bližini vodikovih atomov in elektrofilne regije blizu kisikovih atomov. Intermolekularne interakcije smo raziskali s pomočjo Hirshfeldove analize površine, ki kaže, da prevladujejo interakcije vodikov (O···H/H···O, C···H/H···C, and H···H), ki prispevajo 89,3 %. Po drugi strani pa je analiza nekovalentnih medmolekulskih interakcij (NCI-RDG) pokazala na van der Waalsove interakcije, kar nakazuje na sterične ovire obročev. Da bi ugotovili potencialno učinovitost EMBTh proti ekcemu, smo izvedli tudi študijo molekulskega sidranja; ugotovitve kažejo, da obstaja signifikantna inhibicijska afiniteta na receptor (IL-4Ra) z vrednostjo –7.2 kcal/mol, kar kaže na terapevtski potencial EMBTh glede na tarčni protein, udeležen pri atopičnem ekcemu.



Except when otherwise noted, articles in this journal are published under the terms and conditions of the Creative Commons Attribution 4.0 International License